ORIENTAL JOURNAL OF CHEMISTRY
An International Open Access, Peer Reviewed Research Journal
www.orientjchem.org
ISSN: 0970-020 X
CODEN: OJCHEG
2024, Vol. 40, No.(4):
Pg. 952-965

Unique Magnetically Separable $MnFe_2O_4$/HAP Nanocomposite Photocatalyst for the Removal of Dye Pollutants

ANNETTE JAYAM SOMASUNDARAM and I. SHARMILA LYDIA*

Department of Chemistry, Bishop Heber College (Autonomous), Affiliated to Bharathidasan University, Tiruchirappalli, 620017, Tamil Nadu, India.
*Corresponding author E-mail: sharmilalydia1966@gmail.com

http://dx.doi.org/10.13005/ojc/400405

(Received: May 03, 2024; Accepted: July 18, 2024)

ABSTRACT

In this present work, co-precipitation approach was employed to produce manganese ferrite ($MnFe_2O_4$) nanoparticles and hydroxyapatite (HAP) obtained from microwave assisted co-precipitation method was loaded on the synthesized $MnFe_2O_4$ to produce $MnFe_2O_4$/HAP nanocomposite which is used for the application as photocatalyst. The appearance of sharp peaks in the XRD diffractogram for $MnFe_2O_4$ shows high degree of crystallinity. The presence of flaky spherical agglomerate morphology was confirmed through SEM analysis. The distinct and sharp peaks at 563 cm^{-1} and 411 cm^{-1} in the FT-IR spectra confirm the presence of ferrite phase. Diffuse reflectance analysis confirms that the as prepared photocatalysts absorb light in the visible region. The energy gap values of as-synthesized $MnFe_2O_4$ nanoparticles and $MnFe_2O_4$/HAP nanocomposite calculated using Tauc plot were found to be 1.7 eV and 1.5eV respectively. Photocatalytic activity of $MnFe_2O_4$ and $MnFe_2O_4$/HAP nanocomposites was ascertained for BV3 dye degradation under the illumination of visible light in aqueous solution. The results revealed that the degradation efficiency of 85.35 % and 93.24 % was achieved with $MnFe_2O_4$ nanoparticles and $MnFe_2O_4$/HAP nanocomposite respectively owing to the higher crystallinity and simultaneous adsorption capacity of $MnFe_2O_4$/HAP nanocomposite photocatalyst compared to $MnFe_2O_4$ nanoparticles.

Keywords: $MnFe_2O_4$, Hydroxyapatite, Basic violet 3, Phytotoxicity.

INTRODUCTION

The escalated population combined with speedy development and modernization have worsened the accessibility of fresh water. The polluted water discharged exclusively from textile, printing, leather and dye industries pose severe threat to human and other forms of life. The main contaminants are colourants, and their removal is a paramount concern and a challenging task for researchers[1-2]. Approximately 14% of the total global production of these colourants are being constantly mixed with water bodies. The cationic dyes are more virulent than the other types of dyes ascribable to their harmfulness and the presence of plenty of non-localized pi electrons in the aromatic ring system[3]. The removal of dye molecules from industrial wastewater prior to their release into waterbodies is crucial in the current scenario. The practical feasibility of remediation using the conventional

techniques such as biological, chemical and physical methods seems to be unfruitful due to sludge formation, high operational cost and formation of secondary metabolites[4]. For complete and partial mineralization of dye molecules, advanced oxidation process namely photocatalytic degradation can be a wonderful process for the removal of colourants from the contaminated industrial effluent water[5]. Hence research is being oriented to develop cost effective visible light responsive heterogeneous photocatalysts.

Among the plentiful metal-oxide based photocatalysts spinel ferrite magnetic nanoparticles are given much importance due to excellent catalytic, magnetic, optical and photocatalytic properties. In addition, ferrite based photocatalysts possess chemical stability and reusability[6]. Su. *et al.,* (2012) developed manganese ferrite via a redox method using H_2O_2 for the decolourisation of methyl violet dye under the radiance of visible light[7]. More magnetic composite materials are functionalized with conducting polymers, carbon-based derivatives etc., where magnetic metal oxide material plays a part as core and the conducting material contributes as the shell, that can be implemented for the destruction of dye molecules. Extensive research is being carried out with core-shell magnetic composites coated with Ag, Au, Si and hydroxyapatite (HAP) to improve sturdiness, environmental friendliness and recyclability[8]. The ferrite substances can be doped with inorganic entities namely hydroxyapatite with massively ameliorate photocatalytic activity of the entire composite as a whole. This doped material namely ferrites/HAP can also have numerous biomedical applications. Zarei *et al.,* (2016) prepared $MnFe_2O_4$/HAP as eco-friendly novel photocatalyst with good recycling ability[9]. Tedsree *et al.,* (2017) prepared core shell $MnFe_2O_4$/HAP and determined its photodegradation capability[10]. Nguyen *et al.,* (2014) have synthesized bifunctional core-shell nanocomposite $MnFe_2O_4$/HAP for photodegradation of methyl violet dye[11]. Core shell structured $MnFe_2O_4$/HAP nanocomposites with enhanced photocatalytic performance by visible light illumination was reported by Xia. Y., & Yin. L. (2013)[12].

Basic violet 3 (BV3) is an organic compound which is used as colourant in textile and paint industries to give deep violet colour to clothes, paints and ink. BV3 is highly harmful to flora and fauna with enduring effects[13-14]. Owing to its toxicity, it has been sorted out to be a model dyestuff in this study. This study focuses on the synthesis of HAP supported manganese ferrite $MnFe_2O_4$/HAP nanocomposite using microwave assisted co-precipitation method without any surfactants, which may possess an immense ability to degrade the organic contaminants. The composite is magnetically separable with much recyclability that can be used for the degradation of model dye BV3 and dyes present in textile industry wastewater. Also, it has been planned to assess the toxicity of the treated water by assessing growth of Vigna radiata.

MATERIALS AND METHODS

Materials

Manganese acetate, and calcium hydroxide were purchased from Nice Chemicals for the use as precursors in the synthesis of $MnFe_2O_4$/HAP and Iron(III) chloride, sodium hydroxide, ammonium dihydrogen phosphate, basic violet 3 were sourced from Merck. All the samples purchased were of analytical grade and used without further purification. Synthesis of $MnFe_2O_4$ nanoparticles: $MnFe_2O_4$ nanoparticles were prepared by co-precipitation method. Firstly, a clear solution was prepared by dissolving 8 g of ferric chloride and 3 g of manganese acetate in deionized water. To this solution, 2M of NaOH was added drop wise under vigorous stirring using magnetic stirrer by fixing the temperature at 70°C and the reaction was carried out for 1 hours. The resulting solution was cooled to 25°C. The brownish-black precipitate of $MnFe_2O_4$ formed was dried overnight in hot air oven at 80°C[15].

Synthesis of Hydroxyapatite (HAP)

Hydroxyapatite was synthesized using microwave assisted co-precipitation method. Exactly calcium hydroxide (1.4 M) and ammonium dihydrogen phosphate (0.84M) solutions were prepared using double distilled water. To the hot $Ca(OH)_2$ solution, ammonium dihydrogen phosphate was added slowly with constant stirring using a magnetic stirrer. When the addition was complete the resulting solution was kept in a microwave oven for 5 minutes. Throughout the experiment, the reaction mixture was maintained at the temperature range of 60°C-80°C until the pH of the reaction mixture becomes basic in nature. The reaction mixture was allowed to run for 5 h at this pH condition. The resulting milky white HAP precipitate was filtered using Whatman filter paper (Grade 40), dried using an oven at 80°C for a day and then finally ground to fine powder[16].

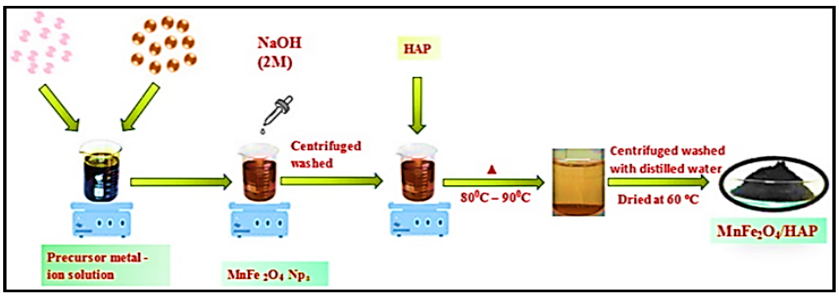

Scheme 1. Synthesis of $MnFe_2O_4$/HAP nanocomposite

Synthesis of $MnFe_2O_4$/HAP nanocomposite

Exactly 4 g of ferric chloride and 1.5 g of manganese acetate were dispersed in 100 mL distilled water to obtain a homogenous mixture. With continuous swirling, lye solution(2M) was supplemented drop by drop to the mixture to form $MnFe_2O_4$ nanoparticles in basic medium (pH=12) and the precipitate was washed with surplus amount of water until the pH turns 7. Thereafter HAP was disseminated into the solution (1:1 mass ratio) with continual stirring to yield a homogenous suspension and it was microwaved for 5 minute. The composite formed was separated by centrifugation, followed by washing with distilled water. Then it was heated in an oven at 80^{O}C for 60 min and cooled. Finally, $MnFe_2O_4$/HAP nanocomposite was obtained[17].

Characterization

PXRD spectrum of the as-synthesized nanocomposite materials was documented using PANalytical/X'pert3 powder diffractometer with λ=0.1541nm Cu-Kα radiation. The surface morphology of the synthesized material was analysed using scanning electron microscope coupled with EDX analyser-FESEM JOEL JSMT300, operated at 10 kV. TEM images were visualized using HitachiH-7500 transmission electron microscope at an accelerating voltage of 200 kV. UV-Vis reflectance data and functional group identification were obtained using Shimadzu-RF 6000 spectrometer and Perkin Elmer-RES-10 spectrum 400 FT-IR spectrometers. PL spectrum was recorded on a fluorescence spectrophotometer at λ_{ext} = 325nm. Magnetic property was analysed on a SQUID-VSM DC magnetometer[18].

Photodegradation Evaluation

The photocatalytic ability of the as-synthesized HAP, $MnFe_2O_4$ nanomaterials, and $MnFe_2O_4$/HAP nanocomposite was examined using BV3 dye solution under the gleam of 30 W LED flashlight. For the discolouration work, fifty millilitres of 1x10^{-4} M experimental solution of BV3 dye was processed with 2 drops of H_2O_2 with different catalyst dosages[19]. After irradiation, 3 mL of dye solution were taken from the suspension and the λ_{max} of the solution was monitored at 587nm which is the λ_{max} of BV3 dye solution[20]. The extensiveness of decolourisation (DD) of the sample was determined by using the relation DD% = $(A_i-A_t)/A_i$ x 100 where A_i is the samples' absorbance at zeroth time and A_t is the absorbance at regular time intervals t.

RESULTS AND DISCUSSION

Determination of crystalline nature by XRD

Powder XRD patterns are used to verify the crystalline nature and average particle size. The XRD peaks of HAP, $MnFe_2O_4$, and $MnFe_2O_4$/HAP nanocomposite photocatalysts are depicted in Fig.1F1(a-c). The XRD pattern of HAP, with the major peaks observed at 2theta are 25.30, 31.84, 32.00, 32.99, 34.12, 39.66, and 49.37 which correspond to (002), (211), (112) (300), (202), (130), and (213) planes of hydroxyapatite respectively. (Fig. 1. F1(a). These angles obtained for HAP agree as per JCPDS File No:24-0033 and therefore the hexagonal crystalline structure of HAP was confirmed. The diffraction pattern of $MnFe_2O_4$ is shown in Fig.1. F1(b) and it catalyst displayed seven characteristic peaks at 2θ equal to 18.02, 29.72, 35.34, 42.68, 53.10, 56.25, and 61.88 which corresponds to the (111), (220), (311), (400), (422), (511) and (440) hexagonal planes of face cantered cubic close packing structure respectively with a lattice constant of 8.470^{O}A which matches exactly with the JCPDS Card No:88-1965[21]. These patterns confirm the spinel structure of $MnFe_2O_4$ magnetic core. Fig.1. F1(c) represents the diffraction pattern of $MnFe_2O_4$/HAP nanocomposite which incorporates the peaks of $MnFe_2O_4$ and HAP. No peaks due to impurities were seen and all the diffraction peaks related to $MnFe_2O_4$ and HAP were also seen in the diffraction

pattern of $MnFe_2O_4$/HAP nanocomposite. These results suggest the coexistence of $MnFe_2O_4$ and HAP without any impurities and the spinel structure of $MnFe_2O_4$ magnetic core remains unaltered after the incorporation of synthesized nanoparticles over $MnFe_2O_4$/HAP which confirmed the protective coating of HAP on $MnFe_2O_4$ surface. The average crystalline size of $MnFe_2O_4$/HAP and $MnFe_2O_4$ nanoparticles were assessed to be 27.2nm to 18.0nm using Scherrer formula, $D = 0.9/\beta\cos\theta$[22], where λ is the wavelength of X-ray, θ the diffraction angle and β is FWHM.

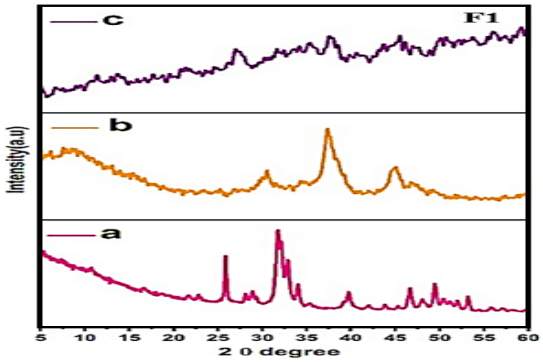

Fig.1. F1. XRD patterns of the synthesized (a) HAP, (b) $MnFe_2O_4$ and (c) $MnFe_2O_4$/HAP nanocomposite

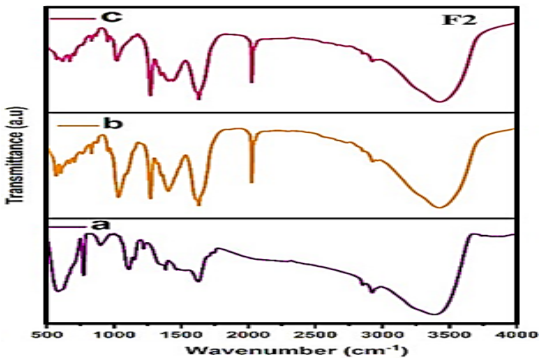

Fig.1. F2. FT-IR spectra of (a) $MnFe_2O_4$ (b) HAP (c) $MnFe_2O_4$/HAP nanocomposite

FT-IR Spectral Studies

Figure 1.F2(a-c) portrays the FT-IR spectra of $MnFe_2O_4$, HAP and $MnFe_2O_4$/HAP nanocomposite. The presence of vibrational peaks (Fig.1.F2a) at 563 cm^{-1} and 411 cm^{-1} confirm Fe-O and Mn-O bonds ascertaining the successful synthesis of $MnFe_2O_4$ nanoparticles with tetrahedral and octahedral sites[23]. Fig.1.F2b shows the FT-IR spectrum of HAP. The H-O-H stretching and bending vibrations at 3418 cm^{-1} and 1626 cm^{-1} indicate the appearance of adsorbed water molecules. The presence of CO_3^{2-} group can be confirmed by the peaks at wavenumbers around 870 cm^{-1} and 1402-1460 cm^{-1} [24]. The bending vibration of O-P-O is the cause of the distinctive phosphate group vibrations of HAP viewed at 567 cm^{-1} and 605 cm^{-1}. The distinct bands at 962 cm^{-1} and 1036 cm^{-1} can be corroborated to symmetric and anti-symmetric stretching vibrations of phosphate group, while the symmetric bending mode of the phosphate group vibration is responsible for the band at 472 cm^{-1}. These results confirmed the formation of HAP[25].

Figure 1. F2c represents the FT-IR spectrum of $MnFe_2O_4$/HAP. The stretching vibrations seen due to the presence of adsorbed water molecules at 3418 cm^{-1} and 1626 cm^{-1} in pure HAP and $MnFe_2O_4$ also appear also in $MnFe_2O_4$/HAP nanocomposite. The sharp FT-IR bands at 2365 cm^{-1} and 2369 cm^{-1} in $MnFe_2O_4$/HAP nanocomposite and in pure HAP are due to the presence of CO_2 which could have come from the air. The distinctive stretching vibrations seen from 600 cm^{-1} to 400 cm^{-1} in $MnFe_2O_4$/HAP nanocomposite indicate the presence of spinel ferrite structure even after, anchoring $MnFe_2O_4$ on HAP matrix[26]. The typical vibrational peak at 565 cm^{-1} accounts for the intrinsic vibration of $MnFe_2O_4$, which overlaps with the stretching vibrations of the phosphate moiety. The vibrational peaks of HAP and $MnFe_2O_4$ could be seen in $MnFe_2O_4$/HAP and the peak shift to the lower frequencies indicate the formation of the $MnFe_2O_4$/HAP nanocomposite requires less energy of vibration. All the results confirm the successful formation of $MnFe_2O_4$/HAP nanocomposite[27].

Morphology and Elemental mapping studies

The microscopic images of $MnFe_2O_4$, HAP and $MnFe_2O_4$/HAP nanocomposite are shown in Fig. 2 with various enhancement. It can be ascertained from the images that $MnFe_2O_4$ nanoparticles exhibit flaky like morphology having a diameter of around 100nm, whereas HAP nanoparticles show rod shaped morphology having a diameter of 200nm. The SEM images of $MnFe_2O_4$/HAP nanocomposite show that $MnFe_2O_4$ nanoparticles are embedded on a flaky sheet structure of HAP. A clear boundary was observed between $MnFe_2O_4$ and HAP sheet and all the small crystallites of $MnFe_2O_4$ nanoparticles were arranged randomly on the surface of HAP. Thus, the decorated $MnFe_2O_4$/HAP nanocomposite demonstrates that $MnFe_2O_4$ nanoparticles are well dispersed[28].

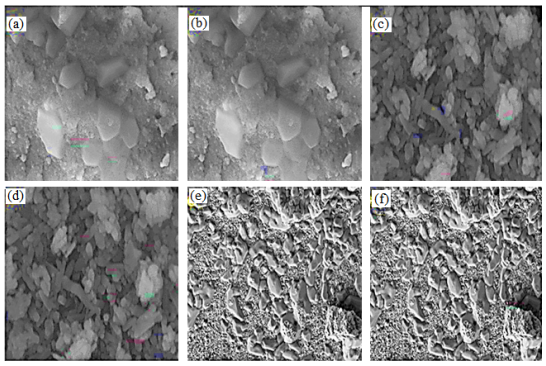

Fig. 2. SEM photographs of (a, b) $MnFe_2O_4$ (c, d) HAP (e, f) $MnFe_2O_4$/HAP nanocomposite

The TEM images confirm the size and distribution of $MnFe_2O_4$ nanoparticles (Fig. 3a) and $MnFe_2O_4$/HAP nanocomposite (Fig. 3b,c) synthesized via co-precipitation and microwave assisted co-precipitation method respectively. The results point out that the particles in the photocatalysts exhibit uniform morphology and distribution. The smallest particle size found for $MnFe_2O_4$ nanoparticles and $MnFe_2O_4$/HAP nanocomposite was 20nm and 50nm respectively. The particle size was increased due to the incorporation of HAP. This suggests that HAP fuse with $MnFe_2O$ to increase the particle size of the $MnFe_2O_4$/HAP nanocomposite. The chemical composition of $MnFe_2O_4$/HAP nanocomposite was identified using the results of EDX investigation and are displayed in Fig. 3d, which authenticate the $MnFe_2O_4$/HAP nanocomposite is constituted with the elements Ca, P, Mn, Fe, C and O atoms. The signal of carbon may be due to the absorption of any organic molecules and thus confirming the absence of any other elemental impurities[29].

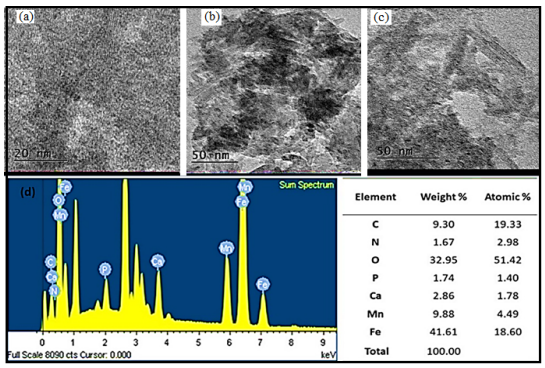

Fig. 3.(a) TEM images of $MnFe_2O_4$ nanoparticles (b, c) $MnFe_2O_4$/HAP nanocomposite and (d)EDX spectrum of $MnFe_2O_4$/HAP nanocomposite

UV-Visible Diffuse Reflectance Spectral Study

The $MnFe_2O_4$ and $MnFe_2O_4$/HAP nanocomposites exhibit strong absorptions from 250nm to 1200nm. The DRS scan spectra and the Tauc plot of $MnFe_2O_4$ and $MnFe_2O_4$/HAP are shown in Fig.4 (a, b). The optical absorption near the band edge can be calculated using the formula $\alpha h\nu = C[h\nu\text{-}E_g]^n$, where energy of the photon (a standard value), and the band gap energy are represented as C and E_g. The variable 'n' is a value obtained for the electronic shift takes place during absorption. The distinct absorption band from 350nm to 1050nm proves that the absorption of visible light can be attributable to the transition takes place in band gap and not caused by absorption due to impurities. Based on the Tauc plot, the E_g values were calculated to be 1.7eV and 1.5eV for $MnFe_2O_4$ and $MnFe_2O_4$/HAP nanocomposite respectively. Owing to the captivating power of ferrites to take up visible light, the band gap values was found to decline from 1.7eV to 1.5eV for the $MnFe_2O_4$ anchored HAP nanocomposite[30].

Photoluminescence

Photoluminescence spectrum of HAP, $MnFe_2O_4$ and $MnFe_2O_4$/HAP nanocomposite was recorded to understand the separation of electron-hole pairs. Fig. 5 presents the photoluminescence sweep of HAP, $MnFe_2O_4$ and $MnFe_2O_4$/HAP nanocomposite. All the three samples were excited at 325nm with Ar^+- ion laser. Bare HAP powder sample showed a broad band centred around 464nm and 520nm due to the presence of thermal activation defects[31]. Under these condition $MnFe_2O_4$ and $MnFe_2O_4$/HAP anocomposites did not show luminescence spectra, demonstrating ferrite-based samples promote the suppression of PL emission of HAP. But when compared to $MnFe_2O_4$ sample, the $MnFe_2O_4$/HAP showed a remarkable lowering of intensity of photoluminescence peak which signifies an effective transfer of charges over $MnFe_2O_4$/HAP nanocomposite matrix and suggesting a significant reduction in recombination ratio of charge carrier. The decrease in the electron-hole recombination process will certainly aid the effective schlepping of electron hole pairs on the surface of the heterojunction, simultaneously elevating

photodegradation efficiency of the magnetic $MnFe_2O_4$/HAP nanocomposite.

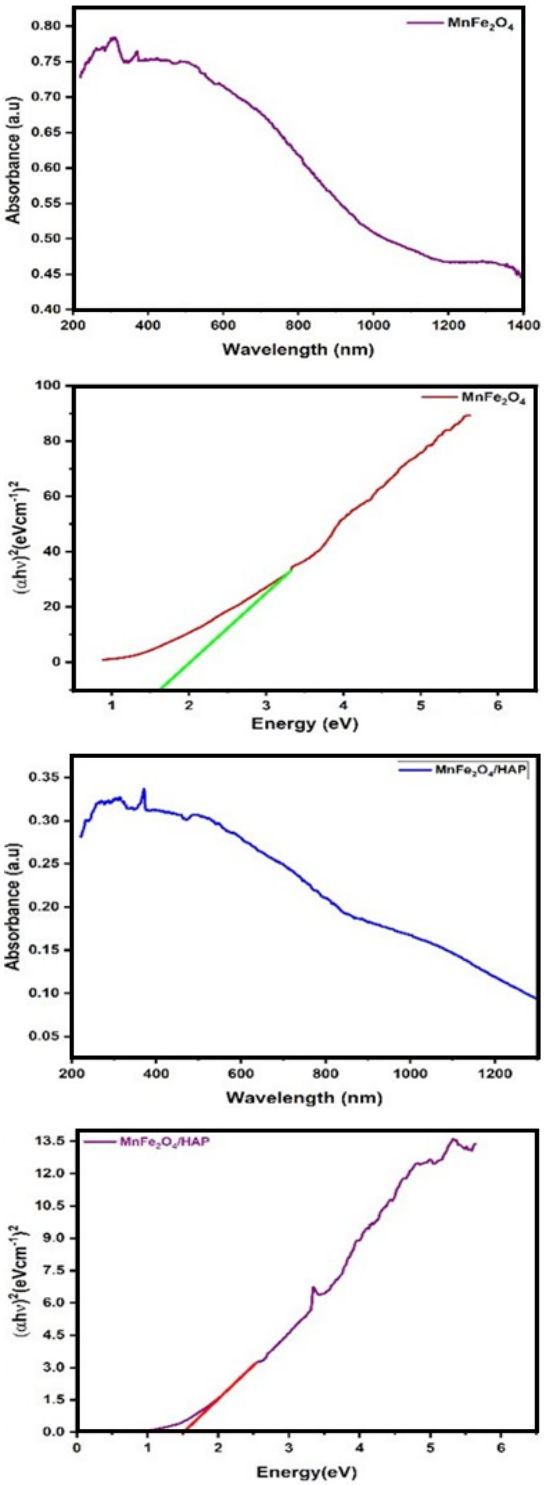

Fig. 4. Diffuse Reflectance spectra and Tauc graph of (a) $MnFe_2O_4$ (b) $MnFe_2O_4$/HAP nanocomposite

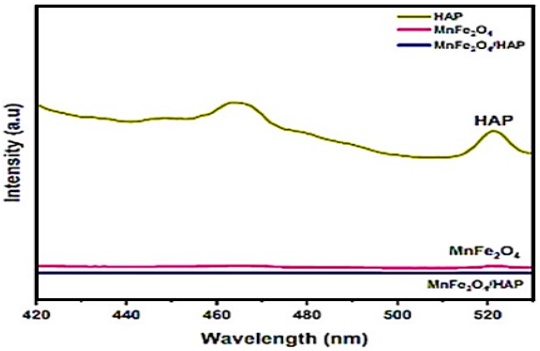

Fig. 5. Photoluminescence spectra: HAP, $MnFe_2O_4$ \and $MnFe_2O_4$ anchored HAP nanocomposite

VSM analysis

The magnetic properties of $MnFe_2O_4$ and $MnFe_2O_4$/HAP nanocomposite were evaluated using vibrating sample magnetometer in the range of -15000 to +15000 O_e at 25^{0}C. Fig. 6 (a, b) shows the plot of saturation magnetization V_s applied magnetic field depicting a small hysteresis loop which denotes that both the samples exhibits typical ferromagnetic or soft magnetic nature. The saturation magnetization (M_s) of $MnFe_2O_4$ and $MnFe_2O_4$/HAP nanocomposite were 8.0 and 1.56 emu/g respectively. The decrease in saturation magnetization value was mainly due to the addition of non- magnetic chitosan material. Though there was a decrease in saturation magnetization value owing to the soft magnetic nature of the $MnFe_2O_4$/HAP composite material, the catalyst could be effectively removed with the use of external magnet from the treated BV3 dye solution.

XPS analysis

XPS analysis was carried out to spot the chemical constituents on the surface and electronic environment of $MnFe_2O_4$/HAP nanocomposite. The XPS investigation and high definition images of $MnFe_2O_4$/HAP nanocomposite are shown in Fig. 7 and Fig. 7(a-f). The results authenticate that the $MnFe_2O_4$/HAP nanocomposite has a polymeric surface comprising Mn2p (531.3 eV), Fe2p (284.9 eV), O1s (642.2 eV), C1s (710.2 eV), Ca2p (347.1 eV) and P2p (133.0 eV) assigned to the sample composition, confirming that $MnFe_2O_4$/HAP nanocomposite has all the expected elements. The observed C1s spectrum (Fig. 7a) of carbon might be due to the precursor acetate used in the synthesis process or air contamination. For $MnFe_2O_4$/HAP nanocomposite the high-resolution O 1s scan portrayed in Fig. 7b can be accredited to the oxygen atom bound with manganese, iron, calcium

and phosphorous atoms owing to the existence of HAP polymeric matrix. Evidently the sharp peaks cantered at 531.4 eV is caused by Fe-O/C-O bonds[33].

Figure 7c presents the high definition XPS spectrum of Fe2p with binding energy at 710.2 eV and 725.9 eV pertained to the energy levels of $Fe2p_{3/2}$ and $Fe2p_{1/2}$ respectively, which are attributed to Fe^{3+} [34]. The representative binding energy at 654.3 eV and 642.2 eV are allocated to the predictable doublets of $Mn2p_{1/2}$ and $Mn2p_{3/2}$ as seen in Fig. 7d. The swapping of Mn for Fe in Fe_3O_4 crystals, for the formation of $MnFe_2O_4$ crystals was further verified by the results of XPS spectra of Fe2p and Mn2p characteristic peaks. The high definition XPS scan of Ca2p for $MnFe_2O_4$/HAP nanocomposite exhibit duplet peaks appertained to the binding energy values 350.6 eV and 347.1 eV of Calcium $2p_{1/2}$ and Calcium $2p_{3/2}$ (Fig. 7e) respectively. The peak viewed around 347.1 eV validate the existence of $Ca2p_{3/2}$ which in turn corroborate that the calcium atoms are tethered to PO_4^{3-} groups[35]. Eventually, the P2p XPS high resolution scan demonstrated duplet peaks, with the energy levels for $P2p_{3/2}$ at 133.8 eV and for $P2p_{1/2}$ at 133.0 eV which could be correlated to the Phosphorous-Oxygen bond in hydroxyapatite (Fig. 7f)[36]. Therefore, based on the XPS analysis $MnFe_2O_4$/HAP nanocomposite has been favourably fabricated via the synthetic procedure followed in this study.

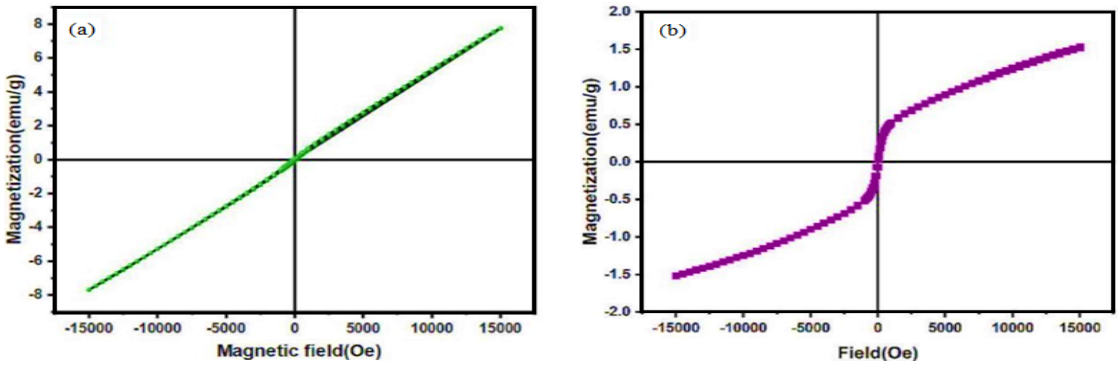

Fig. 6. Magnetic hysteresis curves: (a) $MnFe_2O_4$ and (b) $MnFe_2O_4$/HAP nanocomposite

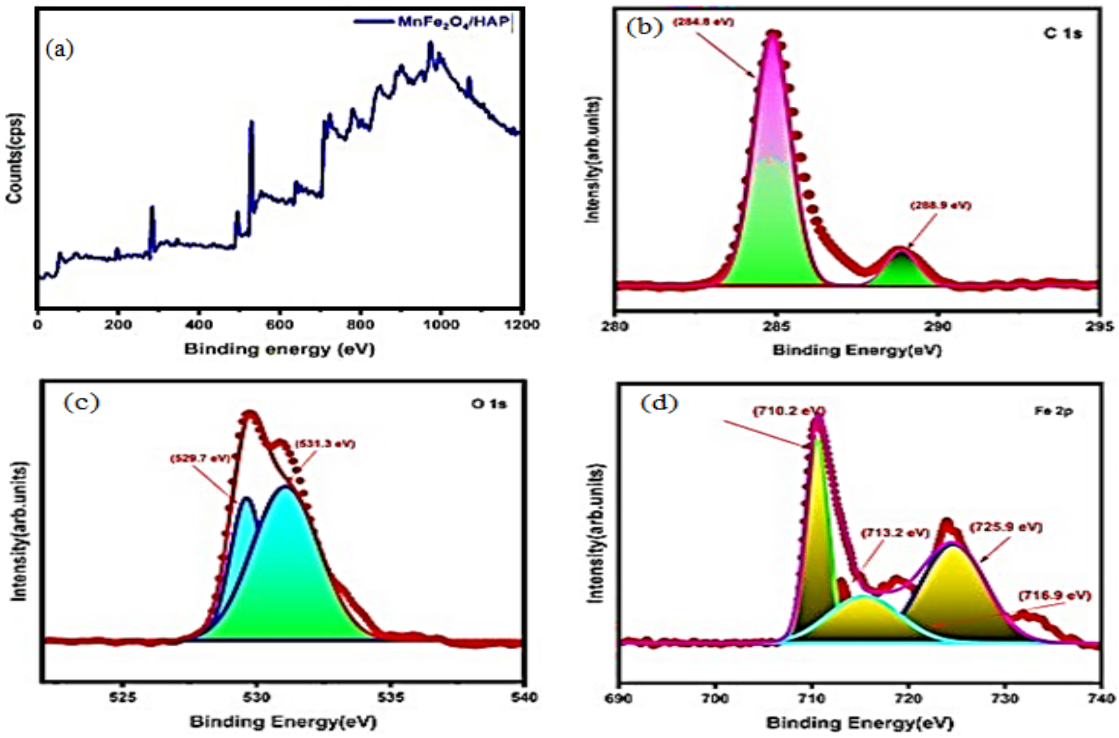

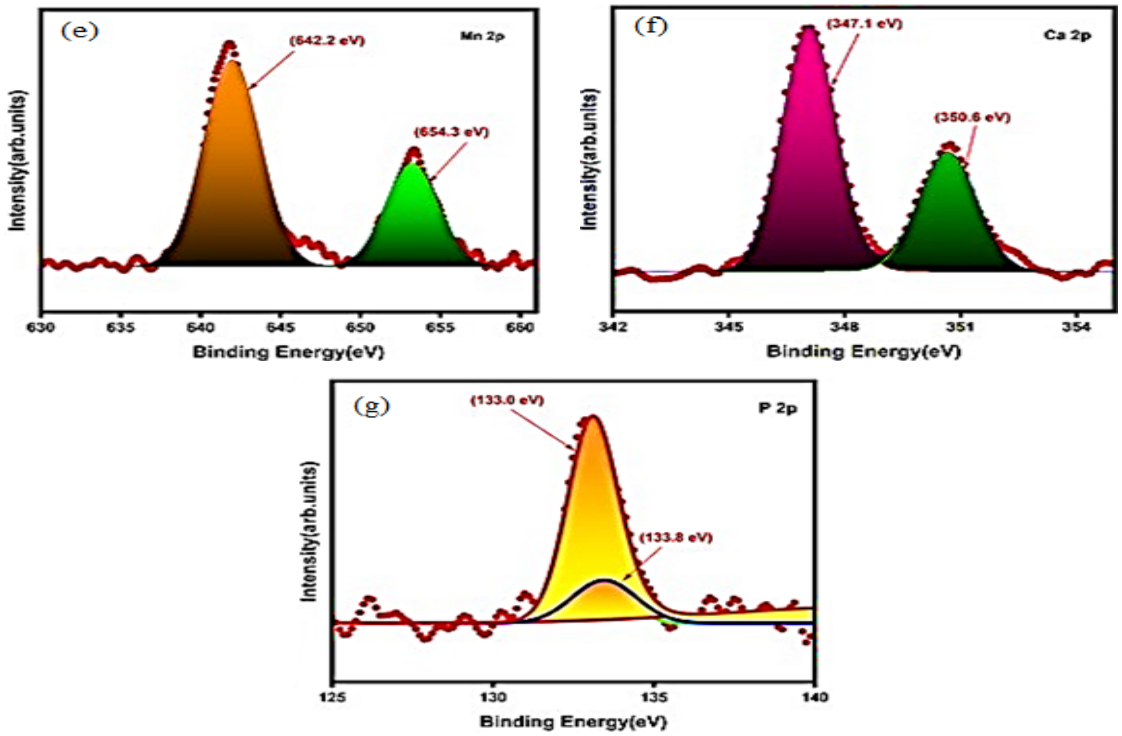

Fig. 7. XPS survey spectrum of $MnFe_2O_4$/HAP nanocomposite, (a-f) High magnification XPS spectra of $MnFe_2O_4$/HAP nanocomposite (a) Carbon 1s (b) Oxygen 1s (c) Iron 2p (d) Manganese 2p (e) Calcium 2p and (f) Phosphorous 2p

Photocatalytic degradation of BV3

The photodegradation ability of the as-fabricated $MnFe_2O_4$ and $MnFe_2O$/HAP nanocomposite was tested by degrading BV3 dye aqueous solution by the illumination of visible light. The BV3 dye degradation in the dark was minimal, ie., 11.25%, as depicted in Fig. 8. It is obvious that visible light irradiation is required for the BV3 dye solution to undergo photodegradation. A degradation efficiency of 14.64% for BV3 dye was observed using LED flashlight light illumination, which substantiate that only minimum degradation was achieved where the mineralization reaction was exposed to LED light without any photocatalyst. Additionally, a second set of degradation of BV3 dye solution was conducted using the as-synthesized $MnFe_2O_4$ and $MnFe_2O_4$/HAP nanocomposite. After 210 min of visible light illumination, BV3 dye degradation was assessed to be 85.35% and 93.24% for $MnFe_2O_4$ and $MnFe_2O_4$/HAP nanocomposite respectively[37]. It is worthy note to mention that $MnFe_2O_4$/HAP nanocomposite exhibited higher photocatalytic activity owing to adsorption and photodegradation processes.

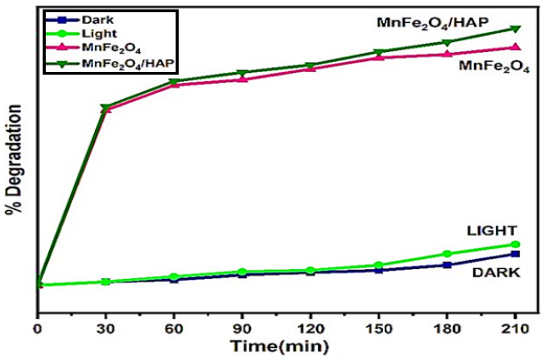

Fig. 8. Photocatalytic degradation of BV3 dye aqueous solution under Dark, Light, $MnFe_2O_4$, $MnFe_2O_4$/HAP. [BV3] = $1x10^{-4}$ M, pH=7, Temp=34±2°C

The UV-Vis spectral changes for BV3 dye degradation during the photocatalytic treatment with $MnFe_2O_4$ and $MnFe_2O_4$/HAP nanocomposite under visible light illumination are highlighted in Fig. 9(a,b). The characteristic absorption band of BV3 dye at 587nm is monitored at regular intervals of visible light illumination for the entire irradiation time of 210 minute. The distinctive absorption peak of BV3 monitored around 587nm gradually decreases and finally a flattened curve was seen after 210 min making

$MnFe_2O_4$/HAP nanocomposite, an effective photocatalyst for the elimination of BV3 dye (Fig. 9b)[38]. As there were no additional peaks formed due to the mineralization of BV3 dye, it is understandable that the BV3 dye has been mineralized absolutely.

The concentration of the catalytic material holds an indispensable role in generating the active species to react with the oxidants, which results in the better photodegradation rates. The consequence of the photocatalyst concentration on the quickness of photocatalytic degradation was assessed by adding 10 mg to 50 mg of catalysts namely $MnFe_2O_4$ and $MnFe_2O_4$/HAP nanocomposites into BV3 dye aqueous solution. As seen in Fig. 9(c, d) the degradation has occurred only after the addition of the photocatalysts and the speed of degradation efficiency has increased with the increase in the catalyst concentration to the extent of 30 mg/50 mL and thereafter a decrease in rate was noticed, for an increase of catalyst concentration to 50 mg/mL[39]. According to Fig. 9(c, d), the degradation efficiency $MnFe_2O_4$ and $MnFe_2O_4$/HAP showed 85.35% and 93.24% dye removal respectively after 210 min of irradiation using 30 mg catalyst. The decrease in percentage degradation might be related to the dissemination of light and shielding effect by the cluttering of the higher catalyst concentration, causing opacity acting as an obstacle for visible light absorption, resulting in decreased photodegradation ability[40]. Thus, the optimal catalytic dosage of 30 mg/mL is employed in this work.

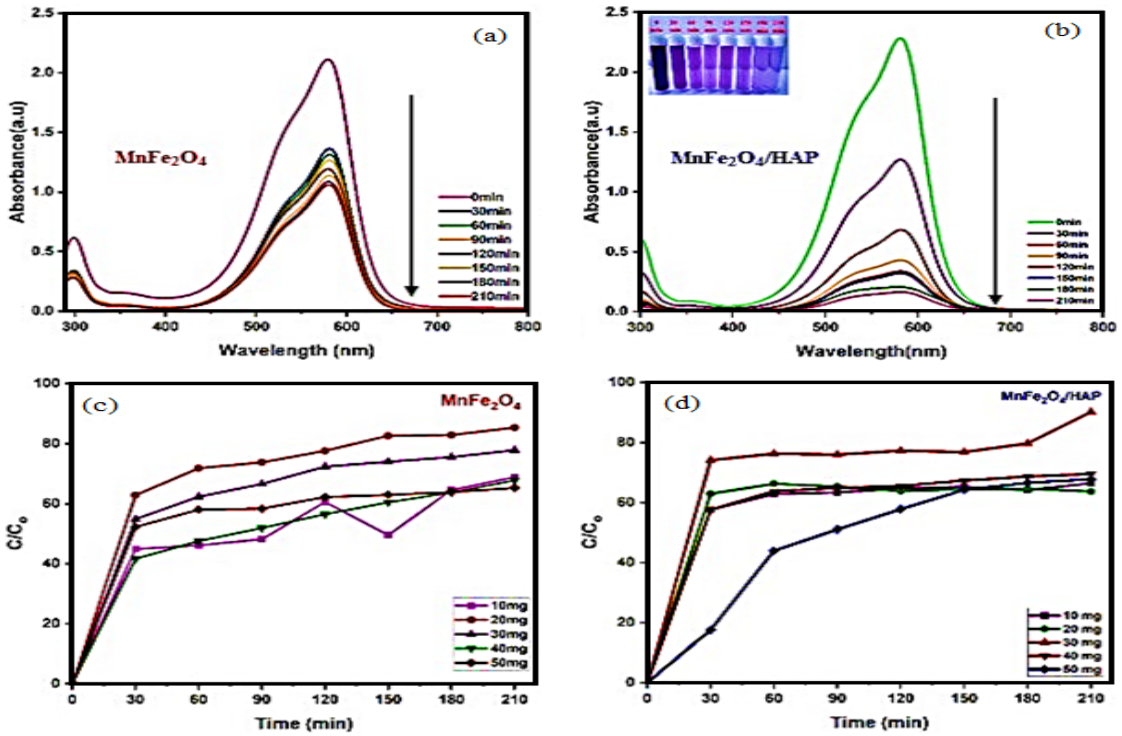

Fig. 9. Changes in absorption scan for the BV3 dye degradation with the use of (a) $MnFe_2O_4$ (b) $MnFe_2O_4$/HAP nanocomposite (c) Effect of various catalyst dosages of $MnFe_2O_4$ and (d) $MnFe_2O_4$/HAP nanocomposites on BV3 degradation

The effect of visible light photodegradation of BV3 dye under four different initial dye concentrations, viz 1x 10^{-4} M, 2x10^{-4} M, 3x10^{-4} M, 4x10^{-4} M, and 5x10^{-4} M was evaluated (Fig. 10a) with $MnFe_2O_4$/HAP nanocomposites. It is noted from Fig.10a, that the rate of photodegradation is decreased with increased concentration of the BV3 dye solution for both the catalysts. The reason is that, greater extent of BV3 dye molecules are adhering on the exterior surface of $MnFe_2O_4$/HAP nanocomposites that can prevent light absorption, thereby lowering the production of photogenerated charge carriers (e^- and h^+). Hence, the degradation efficiency is more at low concentration of BV3 dye[41].

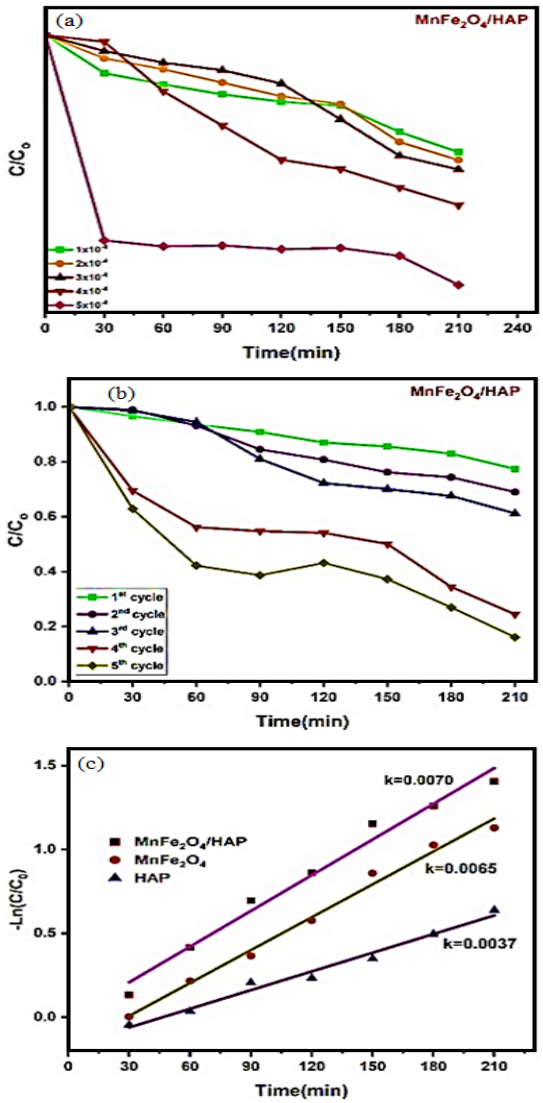

Fig. 10. Influence of BV3 dye initial concentration on BV3 dye molecules degradation using (a) $MnFe_2O_4$/HAP nanocomposite, (b) Reusability of $MnFe_2O_4$/HAP nanocomposite and (c) Kinetic plot of ln (C_o/C_t) Vs irradiation time for BV3 dye degradation using HAP, $MnFe_2O_4$, and $MnFe_2O_4$/HAP nanocomposite under visible light irradiation for 210 minute. [BV3] =1x10^{-4}M; [catalyst] = 30 mg/50 mL

Reusability cycles of $MnFe_2O_4$/HAP for BV3 degradation

The stability of the $MnFe_2O_4$/HAP nanocomposite is examined by performing five cycles of BV3 dye degradation under optimal conditions. The as-fabricated photocatalytic material was retrieved after each cycle, washed thrice, dried, and used for further cycles. The degradation efficiencies of the first, second, third, fourth, and fifth cycles were 75%, 67%, 63%, 31%, and 22% respectively which are shown in Fig. 10b. The findings demonstrated that the degradation efficiency was good across three successive cycles, demonstrating the synthesized catalyst $MnFe_2O_4$/HAP is robust and reusable[42].

Kinetic Analysis

The kinetic Langmuir-Hinshelwood expression, ln C_0/C_t = kt is used to predict the photodegradation rate of BV3 dye solution, where k denotes the rate constant for photodegradation of BV3 dye, C_o stand for the concentration of BV3 prior to irradiation, C_t stand for the concentration of BV3 at the radiance time, t. Fig. 10(c), depicts a straight line for the kinetic plot of ln C_o/C_t Vs time (t) for HAP, $MnFe_2O_4$ and $MnFe_2O_4$/HAP nanocomposite indicating that the photo mineralization of BV3 tracks pseudo first order kinetics with the rate constant values 3.7x10^{-2}, 6.5x10^{-2} and 7.0x10^{-2} min^{-1} respectively[43]. The L-H model thus shows that the degradation rate is profoundly controlled by the as-prepared $MnFe_2O_4$/HAP nanocomposite.

COD removal

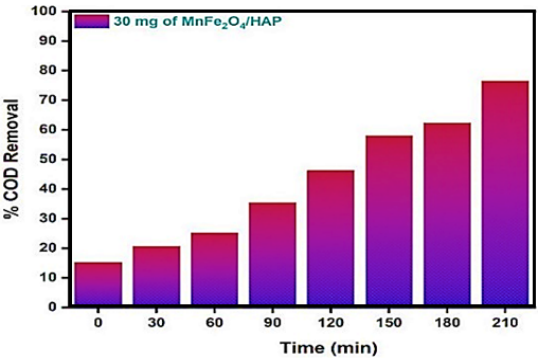

Fig. 11. COD reduction of BV3 dye solution [BV3] = 1x10^{-4}M using 30 mg/50 mL of catalyst at various irradiation time intervals

Chemical oxygen demand was evaluated for BV3 dye degradation in aqueous solution using the $MnFe_2O_4$/HAP nanocomposite by exposing dye solution to illumination. Fig. 11 depicts the percentage removal of COD. The percentage removal of COD reached up to 76% at the end of 210 min, which confirmed the mineralization of BV3 dye[44]. The higher COD removal can be attributed to the simultaneous adsorption and photocatalytic degradation of BV3 dye molecules on the surface of $MnFe_2O_4$/HAP nanocomposite. This could have caused a synergistic effect on the COD removal

caused by the oxidation of BV3 molecules and not because of localized chemical transformations.

Degradation mechanism

The photocatalytic degradation of $MnFe_2O_4$/HAP nanocomposite is believed to occur based on the schematic diagram depicted in Fig. 12. When photons from the visible light are absorbed by $MnFe_2O_4$/HAP, electron and hole pairs (e^--h^+) can be generated within $MnFe_2O_4$/HAP nanocomposite. In the photocatalytic degradation process, the electrons in the valence band are ejected to the conduction band upon irradiation with visible light and the photogenerated holes react with hydroxyl ions leading to the inception of reactive oxygen species i.e., hydroxyl radical, which in turn mineralizes the BV3 dye molecules to harmless products. From O_2 and H_2O molecules, superoxide anion radical (O_2^-) and hydroxyl radical (OH^-) were produced by the interaction of the positive charge of the mesoporous holes with the negative charge of the electrons. In order to break down the adsorbed BV3 dye molecules into smaller molecules of CO_2 and H_2O, these active species of the $MnFe_2O_4$/HAP nanocomposite have formed a strong bond with the positive holes (h^+). Moreover, the rapid mineralization of BV3 dye molecules was enabled by the enhanced adsorption capability of $MnFe_2O_4$/HAP nanocomposite. Furthermore, research has indicated that the greater area specificity of the $MnFe_2O_4$/HAP structure may be the cause of its potent adsorption capabilities[45].

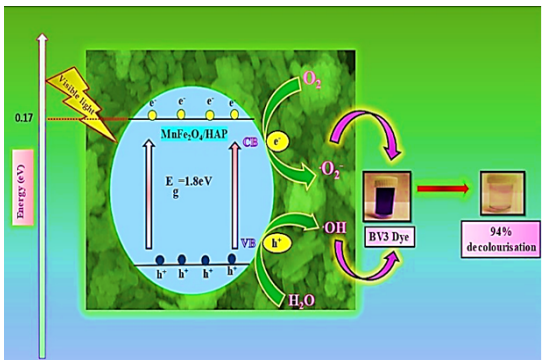

Fig. 12. Plausible photocatalytic pathway of $MnFe_2O_4$/HAP nanocomposite

As a result, $MnFe_2O_4$/HAP would support a solid foundation for its use in hazardous organic dye mineralization. An innocuous and eco-friendly beneficial method of bioremediation for upcoming generations certainly involve the extensive manufacture of $MnFe_2O_4$/HAP with a splendid mesoporous structure using biotic substrates like fish shells, fish bones and egg shells. HAP also possesses strong photocatalytic activity for eliminating azo dye from contaminated waste water. The as-fabricated photocatalysts' enhanced photocatalytic activity is confirmed by the photocatalytic activity data, indicating that the degradation mechanism indicated by a sequence of Eqs. (1-6) is directly caused by this semiconductor ferrite-based nanocomposite.

$$MnFe_2O_4 + h\upsilon_{(visible)} \rightarrow e^-_{(CB)} + h^+_{(VB)} \quad (1)$$

$$e^-_{(CB)} + H_2O_2 \rightarrow {\cdot}OH + OH^- \quad (2)$$

$${\cdot}OH + BV3 \rightarrow \text{Degradation products} \quad (3)$$

$$h^+_{(VB)} + H_2O_2 \rightarrow HO_2{\cdot} + H^+ \quad (4)$$

$$HO_2{\cdot} \rightarrow O_2{\cdot} + H^+ \quad (5)$$

$$O_2{\cdot} + BV3 \rightarrow \text{Degradation products} \quad (6)$$

Phyto toxicity analysis

Vigna radiata is a common bio-indicator utilized primarily for virulency studies. This plant can be easily cultured in laboratory because of having good sensitivity to toxicants. The toxicity of the control solution, treated BV3 dye solution and untreated BV3 dye solution towards the harvest of *Vigna radiata* to explore the harmfulness of BV3 dye solution after photodegradation reactions[46]. Therefore, the seeds *Vigna radiata* plant were chosen and cultivated in treated BV3 dye solution, untreated BV3 dye solution and control sample (Cauvery water). The $MnFe_2O_4$/HAP nanocomposite photocatalysts was able to degrade 93% of BV3 dye solution. The photocatalytic degradation of the mixture is still incomplete as their COD removal is only 76% and it is noteworthy to mention that the intermediates formed due to dye degradation could be deadliest than the BV3 dye molecules. Henceforth, assessing the toxicity of the treated BV3 dye solution is therefore crucial and essential. Fig. 13 portrays *Vigna radiata* plant images grown in control sample, treated BV3 dye solution and untreated BV3 dye solution. The *Vigna radiata* plant grown in control sample (Cauvery water) was 9.6 cm long, whereas those grown in treated BV3 dye solution and untreated dye solution were about 8.2 cm and 3.4 cm long at the end of 15 days. Results from the treated BV3 dye solution and control sample's growth trend were satisfactory. In comparison to the control sample, it is believed that the treated BV3 dye solution has minimum or no harmful effects. Nevertheless, *Vigna radiata*

cultivated in untreated BV3 dye solution showed no discernible growth, and gradually, 40% of the infant plants dried up, possibly as a result of the BV3 dye molecules' negative effects.

Table 1: Phototoxicity results depicting the growth of *Vigna radiata*

Sample	Petiole Length (cm)				
	2nd Day	6th Day	8th Day	12th Day	15th Day
Control Sample	2.1	4.5	5.4	6.5	9.6
Treated BV3 dye solution	2.5	3.7	4.9	5.8	8.2
Untreated BV3 dye solution	2.1	2.6	2.9	3.1	3.4
	Number of branches				
	2nd Day	6th Day	8th Day	12th Day	15th Day
Control Sample	3	6	8	9	15
Treated BV3 dye solution	3	5	6	9	13
Untreated BV3 dye solution	1	2	2	3	3

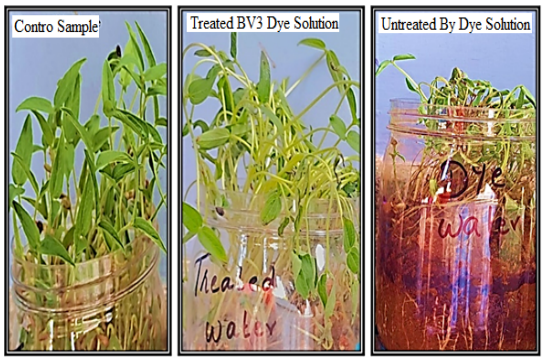

Fig. 13. Digital images of *Vigna radiata* grown in control sample, treated and untreated BV3 dye solution at 25°C at the end of 15 days

These results imply that the untreated BV3 dye solution has persistent toxic effects on the growth and survival of Vigna radiata plant, thus inhibiting its normal growth rate. The treated dye BV3 solution was analysed and was found to contain the non-toxic degradation products such as NH_3, H_2O and CO_2 which was responsible for growth of the plant under study. From the phytotoxicity result, it can be concluded that the toxicity of the treated dye solution using photodegradation process was minimized to a larger extent. Hence, the treated BV3 dye solution was proved to be nontoxic to *Vigna radiata* plant, and can be used without further treatment for domestic and agriculture purposes.

CONCLUSION

In the present study, magnetically separable $MnFe_2O_4$/HAP nanocomposite was carefully prepared by microwave assisted co-precipitation process. Compared with the pure $MnFe_2O_4$ nanoparticles, $MnFe_2O_4$/HAP nanocomposites exhibited higher photoactivity to degrade BV3 dye solution studied under the influence of light illumination. The as-synthesized photocatalytic materials were predicted by XRD, FT-IR, SEM, XPS, UV-DRS, PL and VSM analyses attributing to its structure and morphology. The XRD images authenticate cubic close packing spinel crystalline material with high degree of crystallinity. The characteristic absorption bands in FT-IR spectra confirm the formation of single phase $MnFe_2O_4$. The room temperature VSM analysis ensures the ferromagnetic nature of $MnFe_2O_4$ nanoparticles and $MnFe_2O_4$/HAP nanocomposite material. The photocatalytic competence of $MnFe_2O_4$/HAP nanocomposite to mineralize BV3 dye molecules under the influence of visible light illumination has become notable. Under the optimum conditions the $MnFe_2O_4$/HAP nanocomposite achieved a degradation of 93.24% at the end of 210 min of visible light illumination. The Langmuir-Hinshelwood kinetic plot could logically represent the rate of mineralization of BV3 dye molecules showcasing a surface phenomenon with pseudo-first order rate constants. The reusability study reveals that the $MnFe_2O_4$/HAP nanocomposite can be reused up to three cycles without any significant loss of photocatalytic activity. Phytotoxicity results demonstrated that the treated BV3 dye water has a very little toxic effect in the growth of *Vigna radiata* plant. The findings of this study provide valuable insights for utilizing $MnFe_2O_4$/HAP nanocomposite in the degradation of industrial effluents discharged specifically from textile and dyeing industries.

ACKNOWLEDGEMENT

The authors sincerely acknowledge HAIF centre, Bishop Heber College, Tiruchirappalli, 620017, Tamil Nadu, India for the technical support.

Conflict of Interest

The content of this paper is the sole responsibility of the authors.

REFERENCES

1. Soliman A. M.; Elsuccary S. A. A.; Ali I. M.; and Ayesh A. I., *Journal of Water Process Engineering.*, **2017**, *17*, 245–255.
2. Jayasantha Kumari H.; Krishnamoorthy P.; Arumugam T. K.; Radhakrishnan S.; and Vasudevan D., *International Journal of Biological Macromolecules.*, **2017**, *96*, 324–333.
3. Reeta Mary I.; Leethiyal R.; Sekar P.; Mangalaraj D.; Viswanathan C., and Ponpandian N., *Materials Today: Proceedings.*, **2019**, *18*, 1729–1734.
4. Hu Z. G.; Zhang J.; Chan W. L.; and Szeto Y. S., *Polymer.*, **2006**, *47*(16), 5838–5842.
5. Wojnárovits L.; Pálfi T., and Takács E., *Radiation Physics and Chemistry.*, **2007**, *76*(8–9), 1497–1501.
6. Hema E.; Manikandan A.; Karthika P.; Antony S. A., and Venkatraman B. R., *Journal of Superconductivity and Novel Magnetism.*, **2015**, *28*(8), 2539–2552.
7. Su L.; Feng J.; Zhou X.; Ren C.; Li H., and Chen X., *Analytical Chemistry.,* **2012**, *84*(13), 5753–5758.
8. Ramli R. A.; Adnan R.; Bakar M. A., and Masudi S. A. M., *J. Phys. Sci.*, **2011**, *22*(1), 20-37.
9. Zarei Z., and Akhlaghinia B., *RSC Advances.*, **2016**, *6*(108), 106473–106484.
10. Tedsree K.; Temnuch N.; Sriplai N., and Pinitsoontorn S., *Materials Today: Proceedings.*, **2017**, *4*(5), 6576–6584.
11. Nguyen V. C., *Advances in Natural Sciences: Nanoscience and Nanotechnology.*, **2014**, *5*(3), 035014.
12. Xia Y., and Yin L., *Physical Chemistry Chemical Physics.*, **2013**, *15*(42), 18627.
13. Yang Z.; Gong X., and Zhang C., *Chemical Engineering Journal.*, **2010**, *165*(1), 117–121.
14. Jayalakshmi R.; Jeyanthi J., *Microchemical Journal.*, **2019**, *145*, 791–800.
15. Kafshgari L. A.; Ghorbani M., and Azizi A., *Particulate Science and Technology.*, **2018**, *37*(7), 904–910.
16. Joshi P.; Patel C., and Vyas M., AIP Conference Proceedings. **2018**, pubs.aip.org.
17. Algethami J.; Hassan M.; Alorabi A.; Alhemiary N.; Fallatah A.; Alnaam Y.; Almusabi S., and Amna T., *Nanomaterials.*, **2022**, *12*(10), 1631.
18. Guesmi Y.; Agougui H.; Lafi R.; Jabli M., and Hafiane A., *Journal of Molecular Liquids.*, **2018**, *249*, 912–920.
19. Kakavandi B.; Takdastan A.; Jaafarzadeh N.; Azizi M.; Mirzaei A., and Azari A., *Journal of Photochemistry and Photobiology A: Chemistry.*, **2016**, *314*, 178–188.
20. Federation W. E., and Aph Association. American Public Health Association (APHA): **2005**, Washington, DC, USA, 21.
21. Liew K. H.; Rocha M.; Pereira C.; Pires A. L.; Pereira A. M.; Yarmo M. A.; Juan J. C.; Yusop R. M.; Peixoto A. F., and Freire C., *Chem Cat Chem.*, **2017**, *9*(20), 3930–3941. Portico.
22. Bhowmik M.; Kanmani M.; Debnath A., and Saha B., *Powder Technology.*, **2019**, *354*, 496–504.
23. Yang, Z.; Jiang Y.; Yu L. xin, Wen B.; Li F.; Sun S., and Hou T., *Journal of Materials Chemistry.*, **2005**, *15*(18), 1807.
24. Wang S.; Gao H.; Li J.; Wang Y.; Chen C.; Yu X.; Tang S.; Zhao X.; Sun G., and Li. D., *Journal of Physics and Chemistry of Solids.*, **2021**, *150*, 109891.
25. Rocha J. H. G.; Lemos A. F.; Kannan S.; Agathopoulos S., and Ferreira J. M. F., *Journal of Materials Chemistry.,* **2005**, *15*(47), 5007-5011.
26. Ghobadi M.; Gharabaghi M.; Abdollahi H.; Boroumand Z., and Moradian M., *Journal of Hazardous Materials.*, **2018**, *351*, 308–316.
27. Zhou Y.; Xiao B.; Liu S.-Q.; Meng Z.; Chen Z.-G.; Zou C.-Y.; Liu C.-B.; Chen F.; and Zhou X., *Chemical Engineering Journal.*, **2016**, *283*, 266–275.
28. Das K. Ch.; Das B., and Dhar S. S., *Water, Air, & amp; Soil Pollution.*, **2020**, *231*(2).
29. Paris E. C.; Malafatti J. O. D.; Moreira A. J.; Santos L. C.; Sciena C. R.; Zenatti A.; Escote M. T.; Mastelaro V. R., and Joya M. R., *Environmental Science and Pollution Research.*, **2022**, *29*(27), 41505–41519.
30. Tatarchuk T. R.; Paliychuk N. D.; Bououdina M.; Al-Najar B.; Pacia M.; Macyk W., and Shyichuk A., *Journal of Alloys and Compounds.*, **2018**, *731*, 1256–1266.
31. André R. S.; Paris E. C.; Gurgel M. F. C.; Rosa I. L. V.; Paiva-Santos C. O.; Li M. S.; Varela J. A., and Longo E., *Journal of Alloys and Compounds.*, **2012**, *531*, 50–54.

32. Kafshgari L. A.; Ghorbani M., and Azizi A., *Applied Surface Science.*, **2017**, *419*, 70–83.
33. Lee D.; Kwon O.-S., and Song S. H., *RSC Adv.*, **2017**, *7*(72), 45595–45600.
34. Yamashita T., and Hayes P., *Applied Surface Science.*, **2008**, *254*(8), 2441–2449.
35. Negrila C.; Predoi M.; Iconaru S., and Predoi D., *Molecules.*, **2018**, *23*(11), 2986.
36. Nelson A. E.; Hildebrand N. K. S., and Major P. W., *Surface Science Spectra.*, **2002**, *9*(1), 250–259.
37. Chen Y.; Huang W.; He D.; Situ Y., and Huang H., *ACS Applied Materials & Interfaces.*, **2014**, *6*(16), 14405–14414.
38. Abroshan E.; Farhadi S., and Zabardasti A., *Solar Energy Materials and Solar Cells.*, **2018**, *178*, 154–163.
39. Hou P.; Shi C.; Wu L., and Hou X., *Microchemical Journal.*, **2016**, *128*, 218–225.
40. Valizadeh S.; Rasoulifard M. H., and Dorraji M.S.S., *Applied Surface Sci.*, **2014**, *319*, 358–366.
41. Pare B.; Jonnalagadda S. B.; Tomar H.; Singh P.; and Bhagwat V. W., *Desalination.*, **2008**, *232*(1–3), 80–90.
42. Zhang F.; Yin X.; Zhang W., and Ji Y., *Journal of the Taiwan Institute of Chemical Engineers.*, **2016**, *65*, 269–275.
43. Shariffuddin J. H.; Jones M. I., and Patterson D. A., *Chemical Engineering Research and Design.*, **2013**, *91*(9), 1693–1704.
44. Ertugay, N., & Acar, F. N., *Arabian Journal of Chemistry.*, **2017**, *10*, S1158–S1163.
45. Chai Y.; Ding J.; Wang L.; Liu Q.; Ren J., and Dai W.-L., *Applied Catalysis B: Environmental.*, **2015**, *179*, 29–36.
46. Garcia J. C.; de Souza Freitas T. K. F.; Palácio S. M.; Ambrósio E.; Souza M. T. F.; Santos L. B.; de Cinque Almeida V., and de Souza N. E., *Environmental Monitoring and Assessment.*, **2012**, *185*(3), 2179–2187.